



# Evaluation of the charge transfer kinetics of spin-coated BiVO<sub>4</sub> thin films for sun-driven water photoelectrolysis

Simelys Hernández<sup>a,b,\*</sup>, Gianluca Gerardi<sup>a</sup>, Katarzyna Bejtko<sup>b</sup>, Alberto Fina<sup>a</sup>, Nunzio Russo<sup>a</sup>

<sup>a</sup> Applied Science and Technology Department (DISAT), Politecnico di Torino, C.so Duca degli Abruzzi 24, 10129 Torino, Italy

<sup>b</sup> Center for Space Human Robotics (IIT@POLITO), Istituto Italiano di Tecnologia, C.so Trento 21, 10129 Torino, Italy

## ARTICLE INFO

### Article history:

Received 20 September 2015

Received in revised form 3 February 2016

Accepted 25 February 2016

Available online 28 February 2016

### Keywords:

BiVO<sub>4</sub>

Electrochemical impedance spectroscopy

Water splitting

Transient photocurrent

Charge transfer kinetics

## ABSTRACT

The present research work focuses on bismuth vanadate (BiVO<sub>4</sub>) thin films deposited on FTO-coated glass electrodes through the spin-coating technique, and discusses the influence of different film morphologies (dense and porous) on the physicochemical properties and photoelectrochemical (PEC) performance of the as-prepared photoanodes, for the water splitting reaction. The surface recombination phenomenon, which is one of the main issues of BiVO<sub>4</sub>, has been quantified by means of two distinct approaches: transient photocurrent measurements and electrochemical impedance spectroscopy (EIS). This phenomenon has resulted to be higher in the porous material, thus a poorer performance has been observed than in the dense material. In order to increase the BiVO<sub>4</sub> efficiency, a cobalt phosphate (CoPi) catalyst has been photo-electrodeposited onto the best BiVO<sub>4</sub> electrode, employing an optimized technique and a photocurrent of up to 3 mA/cm<sup>2</sup> at 1.23 V vs. RHE under neutral pH and 1 sun irradiation (100 mW/cm<sup>2</sup>) has been achieved. The charge transfer kinetics of the BiVO<sub>4</sub> photoanodes, with and without CoPi, has also been quantified. The beneficial effect of this water oxidation catalyst, as well as the influence of the preparation method on the uniformity of the film and on its actual performance, is discussed in view of its prospective application in a real PEC device.

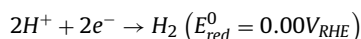
© 2016 Elsevier B.V. All rights reserved.

## 1. Introduction

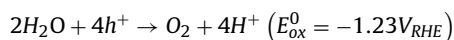
On the path towards an energy transition away from fossil fuels, the development of a device that is capable of efficient water splitting under visible light irradiation remains an important scientific breakthrough that still has to be achieved [1].

Water can be split in a photoelectrochemical cell (PEC), according with the following reduction and oxidation half-reactions [2]:

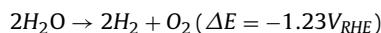
Reduction reaction:



Oxidation reaction:



Overall reaction:



where  $V_{RHE}$  indicates V versus a reversible hydrogen electrode (RHE).

The four-electron water oxidation reaction is the rate-limiting step of the PEC system [3], and the synthesis of an efficient photoanode, capable of overcoming the high over-potential required to perform this reaction, therefore currently represents an important hurdle that has to be overcome.

Among the different metal oxides that have been explored over the last few years [4], bismuth vanadate (BiVO<sub>4</sub>) represents one of the most promising photoanode candidates [5–7]. This metal oxide is an n-type semiconductor, is non-toxic and is composed of inexpensive elements [8,9]. Moreover, it presents three crystal systems: a scheelite structure with monoclinic (s-m) and tetragonal (s-t) phases, and a zirconia structure with a tetragonal (z-t) phase [10]. Owing to the relatively low band gap of ~2.4 eV ( $\lambda < 516$  nm), as well as the suitable levels of the conduction band (CB) and valence band (VB), compared to the water oxidation potential [11], and because of its particular crystal structure [12], the s-m system shows the best activity for O<sub>2</sub> evolution under visible light irradiation [11] and is currently the preferred system for photo-electrochemical applications.

Despite these good properties, BiVO<sub>4</sub> suffers from low charge separation [13] and presents slow transfer kinetics of the photo-

\* Corresponding author.

E-mail addresses: [simelys.hernandez@polito.it](mailto:simelys.hernandez@polito.it), [simelys.hernandez@iit.it](mailto:simelys.hernandez@iit.it) (S. Hernández).

generated carriers to the electrode back contact and across the semiconductor–electrolyte interface [14], which causes a high bulk and surface recombination. As far as photogenerated carrier transport is concerned, electron transport kinetics is known to be limited by the distance between the  $\text{VO}_4$  tetrahedra of the  $\text{BiVO}_4$  crystals, where the V-3d orbitals of the CB lie [13], while hole transfer across the semiconductor–electrolyte interface depends directly on the kinetics of the four-electron oxidation reaction [14]. For this reason, many attempts have been made to enhance the efficiency of  $\text{BiVO}_4$  by inducing structural changes, for example: (i) doping with metals such as Mo and W [15–17]; (ii) the formation of heterojunctions [10,18]; (iii) morphology control [12,19,20] and (iv) co-catalyst deposition [10,21].

The extension of band bending throughout the entire thickness of the  $\text{BiVO}_4$  film with a gradient in a W-dopant concentration, as demonstrated by Abdi et al., is a simple and yet highly effective method, which shows great potential for improvements in charge carrier separation efficiency for higher values than 60% at 1.23  $\text{V}_{\text{RHE}}$  [22]. Another approach explores the possibility of injecting photogenerated electrons into other materials, where they can move faster than in the CB of  $\text{BiVO}_4$  crystals. This approach has been adopted using  $\text{WO}_3$  [18], reduced graphene oxide [23] and Carbon Nanotubes [24].

As far as morphology control is concerned, a photocatalyst with a large surface area generally provides more active sites, promotes an effective separation of the  $\text{e}^-/\text{h}^+$  pairs and also increases light harvesting, due to a multiple scattering effect [25,26]. The small crystal size of s-m  $\text{BiVO}_4$  porous nanostructured powders, which have been used for the photocatalytic degradation of organic matrixes, has allowed a more efficient transfer of the  $\text{e}^-/\text{h}^+$  pairs generated inside the crystal to the surface [27]. However, it has recently been found that a high crystal size is able to enhance the photocatalytic  $\text{O}_2$  evolution activity of s-m  $\text{BiVO}_4$  powders tested under a sacrificial agent (i.e.  $\text{AgNO}_3$ ) [11,19]. Nonetheless, the role of porosity and nanostructuring on s-m  $\text{BiVO}_4$ -based thin films has rarely been investigated in PECs [28].

At the same time, the deposition of an efficient oxygen evolving electro-catalyst (OEC, e.g. based on Co, Fe, Ru or Ir, among others) on the  $\text{BiVO}_4$  surface remains crucial, in order to speed up hole transport across the semiconductor–electrolyte interface [21,29]. In recent years, several studies have demonstrated that cobalt(II)-phosphate complexes (CoPi) can work effectively as OEC in an aqueous phosphate buffer at pH 7, because of the cyclic valence changes of the cobalt ions between  $\text{Co}^{2+}/3^+$  and  $\text{Co}^{3+}/4^+$  [3,30,31]. However, the experimental conditions adopted for the deposition of CoPi, such as the deposition technique (electrodeposition [ED] or photo-electrodeposition [PED]) [21], and the used bias potential [3,32], have a significant effect on the amount (i.e. thickness) of the CoPi film on the electrode surface [14,32], and thus on the efficiency of the photoanode. Therefore, in order to improve photoanode performance, it is of fundamental importance to understand the best combination of experimental conditions that needs to be used for the deposition of CoPi.

In the present work,  $\text{BiVO}_4$  thin films were grown, by means of the spin-coating technique, on transparent conductive substrates, i.e. fluorine-doped tin oxide (FTO) coated glass. Photoanodes with similar thickness, but different morphologies (dense and porous), were synthesized using different annealing processes. The physicochemical characteristics of the synthesised materials were investigated by means of X-ray diffraction (XRD), field emission scanning electron microscopy (FESEM), energy dispersive X-ray spectroscopy (EDX), Raman spectroscopy and UV–vis spectroscopy analyses, and were compared with the photoelectrochemical activity of the different electrodes for the water splitting reaction. In addition, a simple kinetic model, based on the analysis of the normalized transient photocurrent (previously

only applied to  $\text{Fe}_2\text{O}_3$  electrodes), which considers the competition between the interfacial transfer of photogenerated holes and surface recombination [33], was used to investigate how the morphology could affect the water oxidation kinetics on  $\text{BiVO}_4$  photoelectrodes. Moreover, these results were compared with the results extrapolated from electrochemical impedance spectroscopy (EIS) measurements, which were also employed to further elucidate the differences between the two types of  $\text{BiVO}_4$  morphologies, related to electronic transport and charge transfer at the semiconductor–electrolyte interface (i.e. reaction kinetics). The optimal experimental conditions for CoPi PED on a  $\text{BiVO}_4$  photoanode were also investigated, and the beneficial effect of this catalyst was studied by means of both transient photocurrent and EIS methods, as well as through the determination of the flat-band potential ( $E_{\text{fb}}$ ) and donor density ( $N_{\text{D}}$ ) obtained from Mott–Schottky plots [34]. Finally, the influence of the preparation method on the uniformity of the film, and on its actual performance is discussed in view of its prospective application in a real PEC device.

## 2. Experimental

### 2.1. Materials

Bismuth (III) nitrate pentahydrate ( $\text{Bi}(\text{NO}_3)_3 \cdot 5\text{H}_2\text{O}$ ,  $\geq 98\%$ ), vanadyl acetylacetonate ( $\text{VO}(\text{acac})_2$ ,  $\geq 98\%$ ), Cobalt (II) nitrate hexahydrate ( $\text{Co}(\text{NO}_3)_2 \cdot 6\text{H}_2\text{O}$ ,  $\geq 98\%$ ), glacial acetic acid ( $\text{CH}_3\text{CO}_2\text{H}$ ,  $\geq 99.7\%$ ) and acetylacetone ( $\geq 99\%$ ) were used as purchased from Sigma Aldrich. The conductive FTO glasses, with a sheet resistance of  $7 \Omega\text{-cm}^{-2}$ , were obtained from Solaronix Inc.

### 2.2. Synthesis of thin $\text{BiVO}_4$ films

In order to be able to control the morphology and the reproducibility of the  $\text{BiVO}_4$  spin-coated films, a solution of Bi and V precursors dissolved in acetic acid (a weak organic acid) and acetylacetone (a chelating agent) was selected for this work, to avoid the crystallization/precipitation of  $\text{BiVO}_4$  particles in the solution during the spin-coating process (see Section A, Figs. S1 and S2 of the electronic supplementary information, ESI) [25,35]. Thus, two different solutions were prepared, for the synthesis of the  $\text{BiVO}_4$  thin films, by dissolving 1.485 g of  $\text{Bi}(\text{NO}_3)_3 \cdot 5\text{H}_2\text{O}$  in 15 mL of acetic acid and 0.812 g of  $\text{VO}(\text{acac})_2$  in 75 mL of acetylacetone. After pouring the Bi solution into the V solution, the mixture (atomic ratio  $\text{Bi}/\text{V} = 1$ ) was subjected to ultrasonication for 30 min at 59 Hz, after which a very stable solution was obtained; this solution was then employed in the spin-coating procedure. The FTO glass substrates were first cleaned in acetone and ethanol by means of ultrasonication, and then washed with distilled water. The  $\text{BiVO}_4$  deposition process involved a small amount of precursor solution being spread over a  $2 \times 3 \text{ cm}^2$  area in the FTO substrate (previously masked on one side to leave some non-coated FTO available for the electrical contacts) and the substrate was then spin-coated at 500 rpm for 10 s. The film deposition was performed at an ambient temperature of about  $18^\circ\text{C}$  with 22% of relative humidity. After drying at  $150^\circ\text{C}$  for 5 min on a hot plate, the  $\text{BiVO}_4$  coated electrodes were annealed at  $400^\circ\text{C}$  for 10 min and then cooled at room temperature. This procedure was repeated 6 times to increase the film thickness, after which the electrodes were annealed at  $400^\circ\text{C}$  for 2 h. During the thermal treatments, different heating rates were used in order to induce different morphologies on the samples. In order to induce a porous morphology on the  $\text{BiVO}_4$  film, the sample was introduced into an oven already heated to  $400^\circ\text{C}$ ; instead, to induce a progressive sintering of the particles and form a dense film, the sample was introduced into the oven at about  $150^\circ\text{C}$  and then gradually heated at  $2.5^\circ\text{C}/\text{min}$  up to  $400^\circ\text{C}$ .

### 2.3. CoPi photo-electrodeposition

The PED technique was chosen for the CoPi deposition because it provides a more efficient way of coupling CoPi to BiVO<sub>4</sub> photoanodes than simple ED [21,36]. This technique involved the as-prepared BiVO<sub>4</sub> photoanodes (working electrode-WE), an Ag/AgCl (3 M) (reference electrode-RE) and a platinum rod (counter electrode-CE) being immersed in a 0.1 M sodium phosphate (NaPi) buffer containing 0.5 mM of Co<sup>2+</sup> ions (from cobalt nitrate). A constant potential of 1.32 V vs. RHE ( $V_{\text{RHE}}$ ) was then applied for a certain period of time using a multi-channel VSP potentiostat/galvanostat (BioLogic). Simulated solar light (AM 1.5G, 100 mW/cm<sup>2</sup>) from a LUXIM (LIFI-STA-40-01) lamp was used to irradiate the BiVO<sub>4</sub> electrodes during the PED.

In order to establish the optimal amount of CoPi, which is related directly to the photodeposition time, a stepwise PED method was employed on a single BiVO<sub>4</sub> photoanode, alternating a PED bath for CoPi deposition with a Co-free bath for the photoelectrochemical measurements.

### 2.4. Characterization techniques

The BiVO<sub>4</sub> samples were characterized through X-ray diffraction (XRD) using an X'Pert Phillips diffractometer equipped with Cu K $\alpha$  radiation ( $\lambda = 1.5418 \text{ \AA}$ ) at 40 kV and 30 mA. All the patterns were recorded in the 10–60° range, with a step size of 0.02, and the crystallite sizes of the samples were estimated using the Scherrer formula [37,38]. The morphology of the samples was investigated by means of Field Emission Scanning Electron Microscopy (FESEM, ZEISS Dual Beam Auriga), equipped with an Energy Dispersive X-ray spectroscopy system (EDX), which was employed to obtain insight into the actual chemical composition of the sample. Raman spectroscopy was used as it is a technique that can provide structural information and is also a sensitive method for the investigation of the crystallization, local structure and electronic properties of materials. Raman spectra were obtained by means of a Renishaw inVia Reflex (Renishaw PLC, United Kingdom) micro-Raman spectrophotometer, equipped with a cooled charge-coupled device (CCD) camera. Samples were excited with an Ar-Kr laser (514.5 nm). UV–vis absorbance spectra were recorded with a UV–vis spectrophotometer (Lambda 25 by Perkin Elmer) in transmittance mode, using an FTO-covered glass as a reference sample.

### 2.5. Photo-electrochemical tests

The photoelectrochemical characterizations of the BiVO<sub>4</sub> photoanodes (with and without CoPi) were carried out in a 0.1 M NaPi buffer (pH~7), using the previously described three-electrode configuration (BiVO<sub>4</sub> electrode, Ag/AgCl (3 M) and platinum rod). Back-side illumination of the BiVO<sub>4</sub> working electrodes was employed, since higher IPCE spectra have been reported under such conditions than when front-side illumination has been used [13]. Linear scan voltammetries (LSVs) were performed in the dark and under continuous or chopped simulated solar light, using a LUXIM (LIFI-STA-40-01) lamp. The intensity of the light was maintained at 100 mW/cm<sup>2</sup> by adjusting the distance between the source and the PEC. Chrono-amperometry (CA) measurements were performed at 0.6 V vs. Ag/AgCl ( $V_{\text{Ag/AgCl}}$ ) over continuous or chopped visible light irradiation. In order to evaluate the charge transfer resistance across the semiconductor-electrolyte interface, the EIS measurements were conducted in the 0.1 Hz to 0.5 MHz frequency range, with an amplitude of 25 mV, under different applied DC potentials in the 0.3  $V_{\text{Ag/AgCl}}$  to 0.9  $V_{\text{Ag/AgCl}}$  range, with 0.3 V steps. Instead, as far as the Mott–Schottky (M–S) plots are concerned, the EIS measurements were performed at a constant frequency of 5 kHz, with an amplitude of 25 mV, under different applied DC potentials in

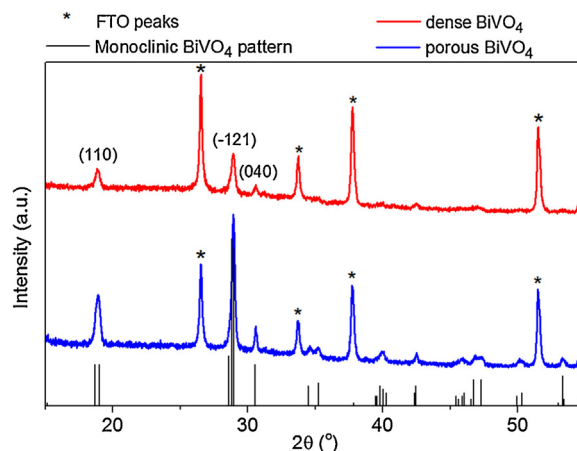


Fig. 1. X-ray diffraction pattern of BiVO<sub>4</sub> thin films with dense and porous morphologies.

the  $-0.6 V_{\text{Ag/AgCl}}$  to  $0.9 V_{\text{Ag/AgCl}}$  range, with 0.1 V steps. The electrochemical data presented in the work refer to the RHE potential calculated with  $V_{\text{RHE}} = E_{\text{Ag/AgCl}} + 0.209 \text{ V} + 0.059 \text{ pH}$ .

## 3. Results and discussions

### 3.1. Structural, morphological and optical investigations of BiVO<sub>4</sub> photoanodes

The XRD spectra of the prepared BiVO<sub>4</sub> films are shown in Fig. 1. All the spectra exhibit the scheelite-monoclinic phase of BiVO<sub>4</sub>, which is characterized by peak splitting at 18.7° and 35° of  $2\theta$ , in good agreement with the values given in the standard Joint Committee on Powder Diffraction Standards (JCPDS) Card No. 14-0688 (space group I2/a,  $a = 5.195 \text{ \AA}$ ,  $b = 11.701 \text{ \AA}$ ,  $c = 5.092 \text{ \AA}$ ,  $\beta = 90.38^\circ$ ). As expected, the z-t phase that could be formed at low temperatures changed to an s-m phase of BiVO<sub>4</sub>, which is considered as the most photoactive for the water oxidation reaction, after calcination at higher temperatures than 400 °C [39].

The top-view FESEM images shown in Fig. 2a–d highlight the different morphologies of the prepared samples, where the nanocrystals are sintered together to form a relatively compact structure, in the case of the so-called “dense film”, while a more porous network of nanocrystals can be observed for the “porous film”. The crystallite sizes distribution of both samples are quite similar, as can be observed from the FESEM micrographs, which is in agreement with the similar crystal sizes estimated using the Scherrer formula from the XRD data: 22 and 27 nm, for the dense and the porous BiVO<sub>4</sub> films, respectively. Such different morphologies, which were desired and induced by the different temperature treatments used during the preparation of the samples (see Section 2.2), are also represented by the different ratios of the most representative XRD peaks of s-m BiVO<sub>4</sub>. Both samples seem to be oriented along the (1 1 0) and ( $-1\ 2\ 1$ ) facets (observed at  $2\theta$ , of about 18.7° and 28.8°, respectively), but such a feature is more marked in the porous material than in the dense one. In fact, the ratio of the intensities of the peaks of the ( $-1\ 2\ 1$ ) and (0 4 0) facets is 2.9 for the porous and 1.7 for the dense film, respectively, while the (1 1 0)/(0 4 0) ratio resulted to be 1.6 and 1.4 for both samples, respectively. Thus, even though the higher exposed surface could play a positive role in the porous film [25,28], the higher fraction of {0 4 0} exposed surfaces in the dense BiVO<sub>4</sub> could be beneficial for water oxidation photo-catalytic activity [11,19], as will be discussed later on. The EDX analyses (see Fig. 2e) have confirmed the presence of Bismuth and Vanadium within the structure, and

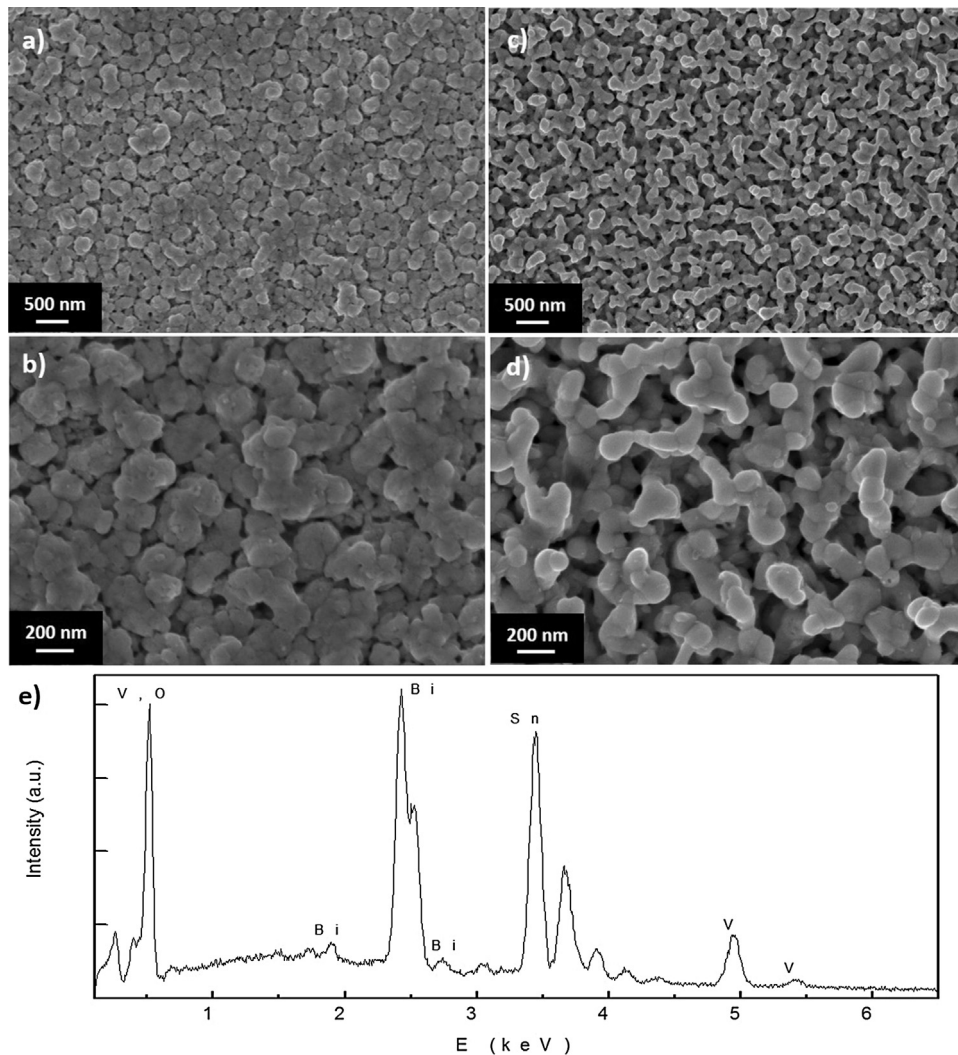


**Fig. 2.** FESEM images of dense (a,b) and porous (c,d)  $\text{BiVO}_4$  thin films on FTO. (e) Representative EDX spectrum of the as-prepared porous film (element Sn derives from FTO-coated glass, probed with the voltage of 12 kV).

the estimated Bi/V atomic ratio is close to one in both samples, thus confirming the stoichiometric composition of the  $\text{BiVO}_4$  films.

The findings of the XRD analysis have been confirmed by the results of the Raman analysis. The Raman spectra of the samples shown in Fig. 3 point out a perfect match with the monoclinic  $\text{BiVO}_4$  structures that have typical vibrational bands at about 210, 324, 366, 710 and  $826 \text{ cm}^{-1}$  (in comparison with RRUFF database of the Raman spectroscopy) [40]. The structural information of  $\text{BiVO}_4$  has been obtained from the band centered at  $210 \text{ cm}^{-1}$ . The asymmetric and symmetric formations of the  $\text{VO}_4$  tetrahedron have been obtained from the bands centered at 324 and  $366 \text{ cm}^{-1}$ , respectively. The stretching modes of the two vibrational modes of the V–O bonds have been determined from the bands centered at 710 and  $826 \text{ cm}^{-1}$ . These two bands provide valuable information on the structural variations in the samples. In fact, a positive shift in the vibrational mode of V–O, which varies from  $824.1 \text{ cm}^{-1}$  on the porous film to  $824.6 \text{ cm}^{-1}$  in the dense one, can be observed. Since the Raman stretching frequencies ( $\nu$ ) and the respective metal–oxygen bond lengths have an inverse relationship, such a shift could be correlated to a variation in the bond length ( $L$ ) of the V–O, which can be calculated by means of Eq. (1) [41]:

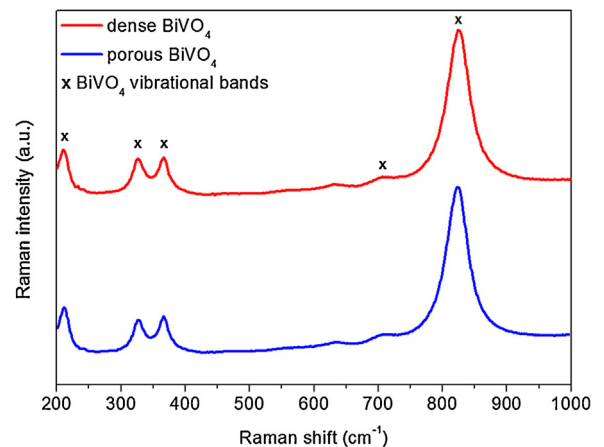


**Fig. 3.** Raman spectra of  $\text{BiVO}_4$  thin films with dense and porous morphologies.

$$\nu[\text{cm}^{-1}] = 21349 \exp(-1.9176 L[\text{\AA}]) \quad (1)$$

It can be seen that the V–O bond length varies slightly, from  $1.6972 \text{\AA}$  in the porous film to  $1.6968 \text{\AA}$  in the dense one. This demonstrates a slight variation in the local crystal structure of the



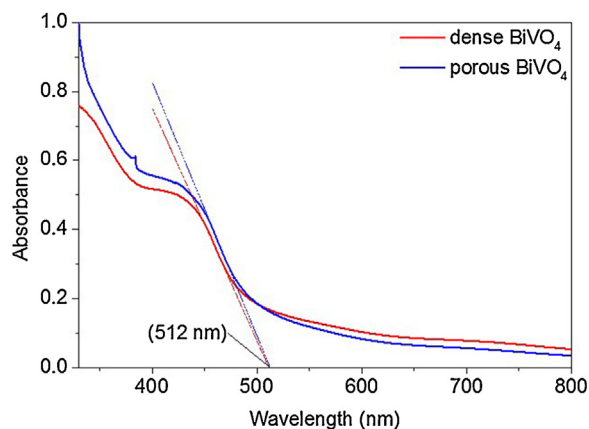


**Fig. 4.** UV-vis absorption spectra of  $\text{BiVO}_4$  thin films with dense and porous morphologies.

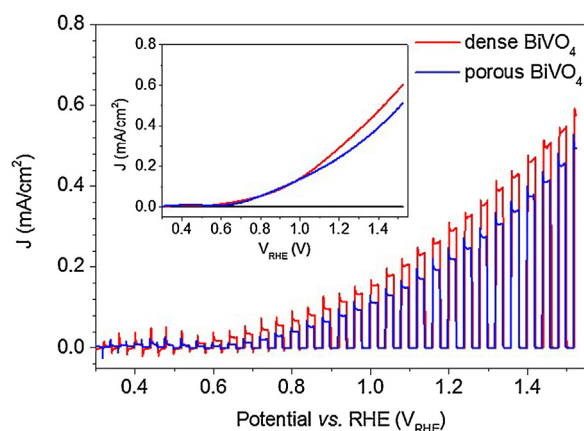


**Fig. 5.** LSV curves of  $\text{BiVO}_4$  thin films with dense and porous morphologies under chopped and continuous (inset) visible light irradiation. The dark signal is reported in black in the inset. Electrolyte: 0.1 M of NaPi buffer; active area:  $6 \text{ cm}^2$ .

samples with the morphology, as the frequencies related to the  $\text{VO}_4$  tetrahedron and V–O bonds are related directly to the interactive forces between the  $\text{Bi}^{3+}$  and  $\text{V}^{5+}$  cations. Such an effect can be explained considering the packing of the structure, and could be correlated to the lone pair distortion around the Bi cation, which has a negative effect on the V–O bond length [42], but plays a positive role in the photocatalytic activity [20,42].

Finally, the UV-vis absorption data presented in Fig. 4 shows absorption in the visible region of the electromagnetic spectrum of the prepared samples, which have a band edge at about 512 nm, corresponding to a band gap of 2.43 eV for both samples, as can be expected for monoclinic  $\text{BiVO}_4$  [11]. In addition, since the absorbance values can be correlated to the quantity of material in the films, it can be affirmed that both the porous and the dense electrodes have similar  $\text{BiVO}_4$  thicknesses (of about 320 nm, see cross-section FESEM image in Fig. S3 of the ESI), as was the purpose of the deposition of 6 spin-coated layers on each sample.

### 3.2. Photoresponse and EIS analysis of $\text{BiVO}_4$ thin films with evaluation of the kinetic constants

The photocatalytic activity of the  $\text{BiVO}_4$  films was evaluated by using them as anodes for the photo-electrochemical water splitting reaction. The LSV curves of the porous and dense  $\text{BiVO}_4$  photoanodes, under chopped illumination, are reported in Fig. 5, which shows how both photoanodes have undergone a certain recombination of the photogenerated  $\text{e}^-/\text{h}^+$  pairs. In fact, in both cases,

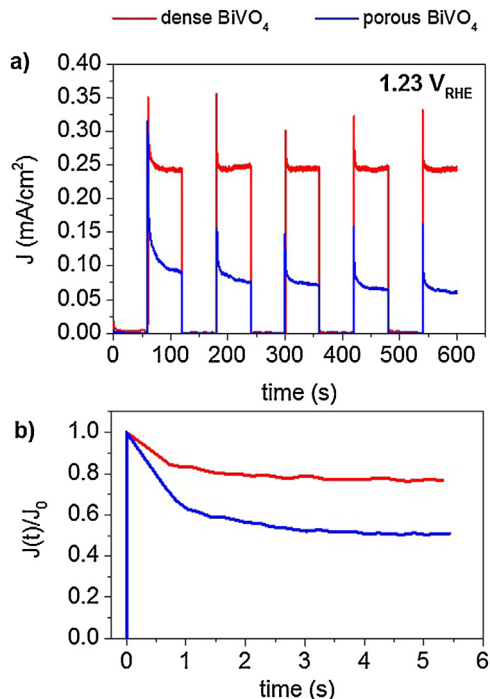


**Fig. 6.** (a) CA curves of  $\text{BiVO}_4$  thin films with dense and porous morphologies under chopped visible light irradiation at a constant applied potential of  $1.23 \text{ V}_{\text{RHE}}$ . Electrolyte: 0.1 M NaPi buffer; active area:  $6 \text{ cm}^2$ . In (b) is shown the fourth normalized photocurrent transients of  $\text{BiVO}_4$  thin films where  $J_0$  represents the photocurrent peak measured when  $t = 0$ .

when the light is turned on, a current peak appears and this is followed by an exponential decay, which is typical of recombination phenomenon [33]. The behaviour of the porous and dense films is very similar under continuous illumination (Fig. 5, inset), with about the same photocurrent onset potential ( $\sim 0.6 \text{ V}_{\text{RHE}}$ ) and equal values of current density until  $1 \text{ V}_{\text{RHE}}$  of applied bias. Instead, for higher voltages, the dense film starts to manifest a higher photoactivity than the porous one, i.e. higher current density values. The difference between the two morphologies becomes much more pronounced when both the LSVs under chopped illumination and the CA curves at a fixed applied bias of  $1.23 \text{ V}_{\text{RHE}}$  (see Fig. 6a) are compared. However, the dense photoanode, in each of the five photocurrent transients measured during the experiment, always demonstrates a higher steady-state photocurrent value than the porous one. Considering that the porous film shows similar or slightly higher UV-vis absorbance than the dense one, and that both  $\text{BiVO}_4$  electrodes have the same crystalline phase as well as similar crystallite sizes, the poorer performance of the porous morphology must be a consequence of its higher recombination rate. Such behaviour would be highly disadvantageous for a real application of such electrodes in a PEC system for continuous  $\text{O}_2/\text{H}_2$  production. Hence, two different approaches were employed to quantify and to obtain detailed information on such recombination phenomena, as well as on the transport and transfer of charges in both types of morphologies.

In the first one, the rate constants related to the surface recombination ( $k_{\text{rec}}$ ) and to the charge transfer across the semiconductor/electrolyte interface ( $k_{\text{tr}}$ ), i.e. to the kinetics for water oxidation reaction, were determined through a simple kinetic model proposed by Peter [33]. This model is based on the evidence that surface recombination is obtained by recording photocurrent-voltage ( $I$ - $V$ ) plots under chopped illumination.

The photocurrent response in the photocurrent onset region shows a characteristic decay, from a 'spike' to a steady state,

**Table 1**

Ratio of kinetic constants and resistance values calculated from either transient photocurrent measurements or EIS analyses.

Material	$k_{tr}/k_{rec}$	$R_s$ [ $\Omega$ ]	$R_{trap}$ [ $\Omega$ ]	$R_{ss}$ [ $\Omega$ ]	$\tau_{ss}$ [ms]
Porous BiVO <sub>4</sub>	0.71	8	132	390	57
Dense BiVO <sub>4</sub>	3.00	13	77	95	14
Dense BiVO <sub>4</sub> -CoPi	5.00	11	54	65	4

during the illumination period, and this is followed by an overshoot and decay back to zero during the dark period, as can be seen in the CA curves in Fig. 6a. Such a phenomenon can be explained by considering that [33] when the light is switched on, the photogenerated electrons and holes are separated, with electrons moving towards the bulk of the semiconductor and holes moving towards the surface. Under continuous illumination, during the 'on' period, the concentration of free (or surface-trapped) holes increases until a steady-state concentration is reached, at which the rate of arrival of the holes is balanced perfectly by the interfacial transfer and recombination. This build-up of holes induces a recombination flux of the electrons towards the surface, which corresponds to a current with an opposite sign to the hole current. In the steady state, the measured photocurrent is the sum of the hole and electron currents.

The time-dependent solution of the problem has already been deduced [43,44]. For the 'on' transient, this solution takes the normalized form:

$$\frac{J(t) - J(\infty)}{J(0) - J(\infty)} = e^{-t/\tau} \quad (2)$$

where  $J$  is the current density at times equals to  $t$ , 0 or at a steady-state ( $\infty$ ), the time constant  $\tau = (k_{tr} + k_{rec})^{-1}$  and the steady-state photocurrent is given by [33]:

$$\frac{J(\infty)}{J(0)} = \frac{k_{tr}}{(k_{tr} + k_{rec})} \quad (3)$$

Thus, the fourth photocurrent transients of the CA experiments were normalized (see Fig. 6b), and the resulting kinetic constants were obtained by resolving Eqs. (2) and (3).  $k_{tr}/k_{rec}$  is reported in Table 1. These results underline how the porous morphology suffers from a higher superficial recombination of the charges, as it has a  $k_{tr}/k_{rec}$  ratio that is about 3 times lower than that of the dense film. Moreover, it is worth noting that the  $k_{tr}/k_{rec}$  ratio is also less than 1 for the porous film, which means that the photogenerated carriers that recombine are greater in number than the ones that are used for the water oxidation reaction in this type of material.

As a second approach, EIS analysis was used as a useful method to study not only the charge transfer at the electrode/electrolyte interface, but also the charge transport in the bulk of the semiconductor. The EIS experimental data recorded at 1.23 V<sub>RHE</sub> (see Fig. 7) were fitted through the equivalent circuit (EC) shown in the inset of Fig. 7, which has already been used to estimate the charge transport and transfer properties of BiVO<sub>4</sub> [5] and Fe<sub>2</sub>O<sub>3</sub> [45,46] electrodes during the water photoelectrolysis reaction.

The EC is constituted by the series resistance  $R_s$  (which accounts for the resistances of the FTO film, the external electrical contacts and the liquid electrolyte); the constant phase element (CPE)  $Q_{bulk}$  (which represents the direct charge transfer at the semiconductor/electrolyte interface); the charge transfer resistance  $R_{trap}$  (which represents the trapping of charges in the surface states); and the parallel between the resistance  $R_{ss}$  (which models the charge transfer between the electrolyte and the surface states) and the surface state CPE  $Q_{ss}$ . CPEs were used instead of common capacitance to take into account the frequency dispersion due to the porosity of the films [47,48]. Hence, this EC considers that the hole transfer mechanism for the water-splitting reaction takes place through surface states [45,46], which could be due to an imperfect interconnection between adjacent layers or crystals in the BiVO<sub>4</sub> film,

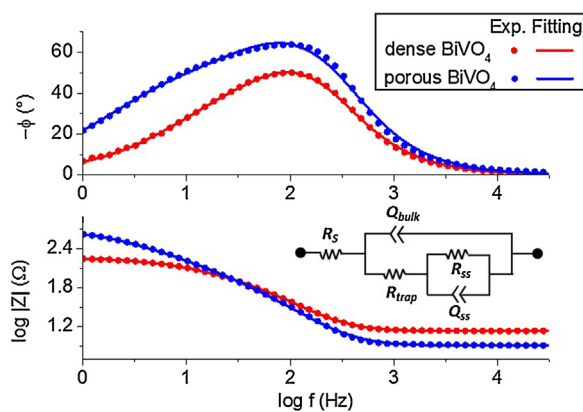


**Fig. 7.** Bode plots of the EIS measurements (symbols) and fitted data (lines) acquired at 1.23 V<sub>RHE</sub> under visible light irradiation (100 mW cm<sup>-2</sup>). Inset: Equivalent circuit adopted for the fitting of EIS data.

induced during the preparation processes, which are constituted by multiple deposition-annealing steps [5], as in the present case.

The good fit can be confirmed from the appropriate overlapping of the experimental and fitted data in the plots shown in Fig. 7. The resulting parameters are reported in Table 1. As expected, the BiVO<sub>4</sub> samples both show similar  $R_s$  values, since they were prepared in the same substrate and were tested under the same experimental conditions. Instead, the porous photoanode shows higher values of both  $R_{trap}$  and  $R_{ss}$  than the dense film. Even though both electrodes have the same quantity of material, the porous BiVO<sub>4</sub> film should provide a higher availability of active surface for the reaction than the dense material and should also induce a higher activity. However, the porous film has a higher resistance ( $R_{ss}$ ) to the charge transfer across the electrode/electrolyte interface, which could be a consequence of an even slower electronic transport than that of the dense morphology, due to the accumulation of e<sup>-</sup> in the surface states (observed as an increased  $R_{trap}$  value). For this reason, moving slowly within the BiVO<sub>4</sub> film to the FTO back contact, the electrons tend to accumulate in the CB and, therefore, to recombine with the holes in the VB, thus giving rise to the reduced photocatalytic activity of the porous BiVO<sub>4</sub> electrode.

The same behaviour is demonstrated by calculating the charge transfer time constant ( $\tau_{ss}$ ) through the following formula [48]:

$$\tau_{ss} = (R_{ss}Q_{ss})^{1/n_{ss}} \quad (4)$$

where  $n_{ss}$  is the CPE index. The porous material in fact exhibits a four times slower  $\tau_{ss}$  (i.e. superficial reaction kinetics) than the dense BiVO<sub>4</sub>, a result that is also in good agreement with the analyses of the transient photocurrents.

The slow transport of electrons is an intrinsic property of the BiVO<sub>4</sub> crystal structure. However, it emerges, from the previous results, that there are other characteristics of the BiVO<sub>4</sub> films, perhaps induced by the preparation procedure, which can also influence its performance, regardless of its available surface area.

In a previous work, for instance, an increase in the annealing temperature (from 350 °C to 800 °C) of s-m BiVO<sub>4</sub> powders induced a reduction in the surface area (due to crystallite agglomeration and an increase in the crystals size), but also an enhanced crystallinity; this leads to a higher delocalization of e<sup>-</sup>/h<sup>+</sup> pairs and a greater overlapping between the Bi 6s and O 2p orbitals. Since, in the band structure of (s-m) BiVO<sub>4</sub>, the VB is formed by means of the hybridization of Bi 6s and O 2p atomic orbitals, while the CB is formed by V 3d atomic orbitals [49], a change in the extent of the overlapping of the Bi 6s and O 2p orbitals occurs in direct proportion to the distortion of the VO<sub>4</sub><sup>3-</sup> tetrahedron, which induces a reduction in the length of the V-O bonds. In turn, this helps the mobility of the photogenerated holes, by reducing the

recombination rate [50] and increasing the  $O_2$  evolution activity [42]. In another case, the interconnection between particles of subsequent dip-coated layers of  $BiVO_4$  has been found to be very important, since grain defects could induce a higher charge carrier recombination and an overall lower activity [5].

Hence, from the previous physicochemical and photoelectrochemical characterizations, it is reasonable to presume that there are different causes behind the poorer performance of the spin-coated  $BiVO_4$  porous film than that of the more compact structure. First, the lower distortion of the  $VO_4^{3-}$  tetrahedron and the higher V–O distance observed from the Raman spectroscopy analysis induces a lower mobility of charge carriers in the porous material. In addition, the higher concentration of defects, which may be induced during the crystallization process, can act as recombination centres at the grain boundaries of the crystals sintered together. Both of these phenomena could be responsible for a higher accumulation of  $e^-$  in the  $BiVO_4$  CB, and could lead to a higher superficial recombination. Finally, the lower fraction of {040} exposed surfaces, noted in the XRD data pertaining to the porous structure, than that of the more compact film, which are known to have a positive influence on the s-m  $BiVO_4$  photoactivity for the water oxidation reaction, may also play a role [12,20,51,52]. However, in the present case, the difference in the (110)/(040) ratios between the two studied materials is too small (i.e. 0.2) to play a predominant role. It is important to remark that these affirmations are not unconditional, and depend on the preparation procedure. In fact, porous  $BiVO_4$  films prepared by means of another physical techniques, e.g. double magnetron sputtering, have achieved photocurrent values of up to  $1.2\text{ mA/cm}^2$  at  $1.23\text{ V}_{RHE}$  [28], which is nearly 4-fold the value obtained with the best of the here presented films.

### 3.3. Optimization of CoPi photo-electrodeposition (PED) on dense $BiVO_4$ thin films: photoresponse and kinetics analyses

In the subsequent tests, co-catalyst deposition was only carried out on the dense  $BiVO_4$  photoanode, due to the better performance it had demonstrated. The cobalt-based catalyst named CoPi was deposited on the sample surface in order to catalyse the water oxidation reaction. The experimental conditions for CoPi PED were optimised (see Section 2.3 for more details) in order to achieve the optimal PED time that maximizes the CoPi activity. In fact, although short PED times lead to small CoPi thicknesses, longer ones reduce the  $BiVO_4$  absorption capacity, with a consequent drastic drop in the photoanode efficiency [32]. As can be seen in Fig. 8, adopting a constant bias of  $1.32\text{ V}_{RHE}$  for the PED, the highest photocurrent has been measured around step 2, which corresponds to a total PED time of about 60 s. Thus, the combination of  $1.32\text{ V}_{RHE}$  and 60 s was then employed to obtain an optimum amount of CoPi on the  $BiVO_4$  photoanode surface.

Since the CoPi catalyst was adopted, the onset potential of the photocatalytic water oxidation reaction on the  $BiVO_4$  was shifted to a lower value (from  $0.6\text{ V}_{RHE}$  to around  $0.4\text{ V}_{RHE}$ ), and an evident improvement in photocurrent generation was observed, as it increased by a factor of 5 (from about  $0.3$  to  $1.4\text{ mA/cm}^2$ , at  $1.23\text{ V}_{RHE}$ , as seen in Fig. 9a).

Interestingly, when the LSV was repeated with a mask on top of the electrode that left a smaller active area ( $0.785\text{ cm}^2$ ) in the centre of the photoanode exposed to the flux of incident photons, the efficiency of the  $BiVO_4$ -CoPi photoanode improved even further, as shown in Fig. 9b. In this case, the photocurrent density was about  $3\text{ mA/cm}^2$  at  $1.23\text{ V}_{RHE}$ , almost 2 times higher than the photocurrent reported in Fig. 9a, which was measured at the same potential but with the whole active area ( $6\text{ cm}^2$ ) of the electrode exposed to the light. Such phenomenon was also observed in the bare  $BiVO_4$  electrode (see the red curves in Fig. 9), and it is therefore likely

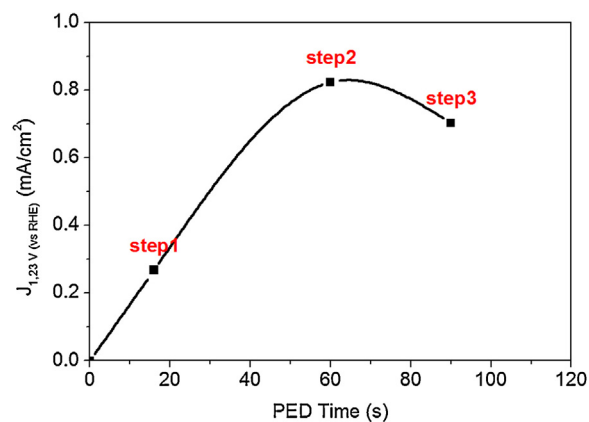


**Fig. 8.** Effect of the successive PED times on the photocurrent generation of a single  $BiVO_4$ -CoPi photoanode. Step1:  $1.32\text{ V}_{RHE}$  for 16 s; step2:  $1.32\text{ V}_{RHE}$  for 48 s and step3:  $1.32\text{ V}_{RHE}$  for 30 s. PED conditions: back-side illumination at  $100\text{ mW/cm}^2$  in  $0.1\text{ M NaPi}$  buffer containing  $0.5\text{ mM Co}^{2+}$ . Photocurrent measurements carried out at a constant potential of  $1.23\text{ V}_{RHE}$  under visible light irradiation; electrolyte:  $0.1\text{ M NaPi}$  buffer.

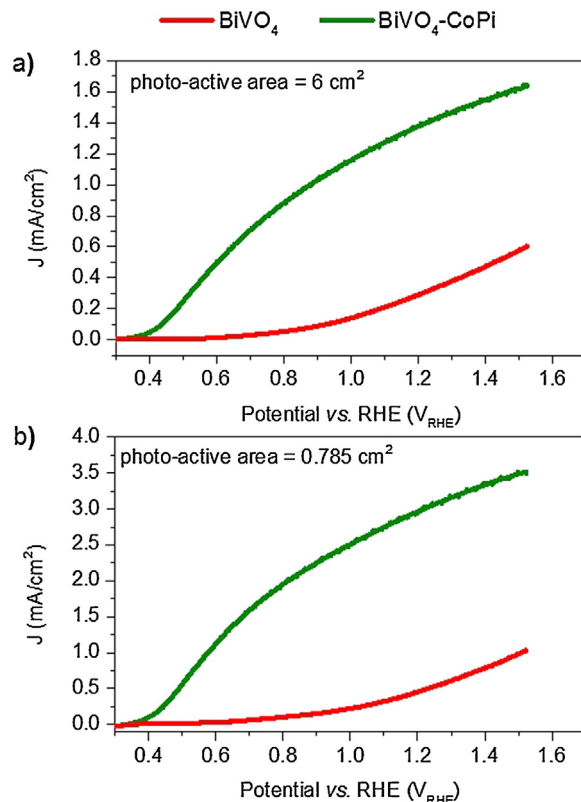


**Fig. 9.** LSV curves of dense  $BiVO_4$  and  $BiVO_4$ -CoPi photoanodes under continuous visible light illumination of all their active area of  $6\text{ cm}^2$  (a) or of their central area of  $0.785\text{ cm}^2$  (b). Electrolyte:  $0.1\text{ M NaPi}$  buffer.

that the discordance between the photocurrent densities does not depend on variable CoPi self-assemblies on the  $BiVO_4$  surface. Such behaviour could be due to a non-homogeneous distribution or quality of the  $BiVO_4$  film over the entire FTO surface. It is important to notice that small areas (about  $1\text{--}2\text{ cm}^2$ ) have usually been reported in most of the works related to the testing of semiconductor photocatalysts in PECs. In the present case, as reported in the ESI (Section B and Fig. S3), the spin-coating process does not induce large differences in thickness, but it can lead to a higher concentration of defective states (i.e. a higher number of grain boundaries produced by a different distribution of the solution when the distance from

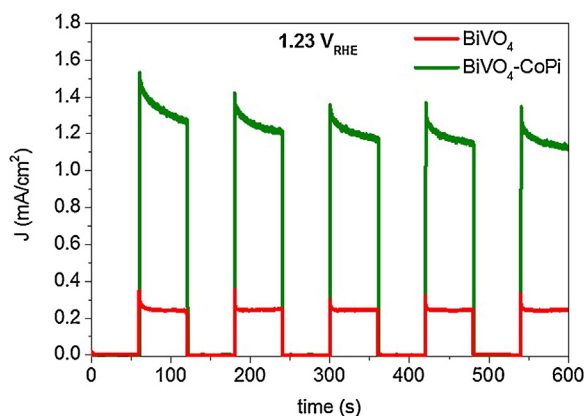


**Fig. 10.** CA curves of dense BiVO<sub>4</sub> and BiVO<sub>4</sub>-CoPi photoanodes under chopped visible light irradiation. Constant applied potential: 1.23 V<sub>RHE</sub>; electrolyte: 0.1 M NaPi buffer; active area: 6 cm<sup>2</sup>.

the centre of the sample increases) at the borders of the large-deposited area. Thus, a difference in the morphology and quality of the BiVO<sub>4</sub> material, between the centre of the electrode (where the light is focused when the covering mask is applied) and the borders of the photoanode, is the main cause of the lower photocatalytic efficiency of the film when the entire 6 cm<sup>2</sup> area is illuminated. This means that, for a practical applications, the spin-coating technique still needs to be optimized in order to have a better control of the homogeneous growth of BiVO<sub>4</sub> films or, alternatively, different techniques should be introduced that would allow a uniform coverage of large surfaces areas, e.g. sputtering or electrodeposition, among others. Nonetheless, the obtained results highlight how coupling of a co-catalysts (such as the CoPi) and BiVO<sub>4</sub> in an optimized way could enable the fabrication of high-performance photoanodes.

The CA reported in Fig. 10 also confirms an almost 6-fold increase in photocurrent generation at a fixed potential of 1.23 V<sub>RHE</sub>. However, the exponential decay from the “on-peak” to the steady state can still be observed in the BiVO<sub>4</sub>-CoPi photoanode, which means that the superficial recombination phenomenon is not totally suppressed by the co-catalyst deposition.

Adopting the same kinetic model described in Section 3.2, the  $k_{tr}/k_{rec}$  ratio was also calculated for the BiVO<sub>4</sub>-CoPi photoanode, and is reported in Table 1. As expected, due to the presence of CoPi, the water oxidation reaction is faster than that of the bare BiVO<sub>4</sub> photoanode, which means that the holes in BiVO<sub>4</sub> VB were quickly consumed at the semiconductor/electrolyte interface and the  $k_{tr}$  value therefore increased, thus leading to a 67% higher  $k_{tr}/k_{rec}$  ratio ( $\approx 5$ ).

In addition, EIS analysis was also performed on the BiVO<sub>4</sub>-CoPi photoanode, and the Bode diagram of this material is reported in Fig. 11, compared with the bare BiVO<sub>4</sub>. From an observation of such a plot, it is evident how the peak of the phase angle ( $-\phi$ ) curve, which indicates how fast the charge transfer at the photoanodes interface occurs, is shifted towards higher frequencies in the case of the BiVO<sub>4</sub>-CoPi photoanode, thus pointing out that the charge transfer phenomenon is faster on such an electrode than on the bare BiVO<sub>4</sub> material. In order to quantify such a phenomenon, the EIS data were fitted using the same EC (see the inset in Fig. 7) and the same procedure explained above. The values obtained for  $R_{trap}$ ,  $R_{ss}$  and  $\tau_{ss}$  are shown in Table 1. The trapping of the charges in the BiVO<sub>4</sub> surface states (where the reaction occurs) decreases, due to the CoPi effect, as can be seen by the reduction in the  $R_{trap}$  value of about 30%. As a consequence, a lower number of  $e^-/h^+$  pairs recombine and the charge transfer across the interface is accelerated by about 70%, as evidenced by the reduction of 32% and 29% on  $R_{ss}$  and  $\tau_{ss}$ , respectively. Such results are in complete agreement

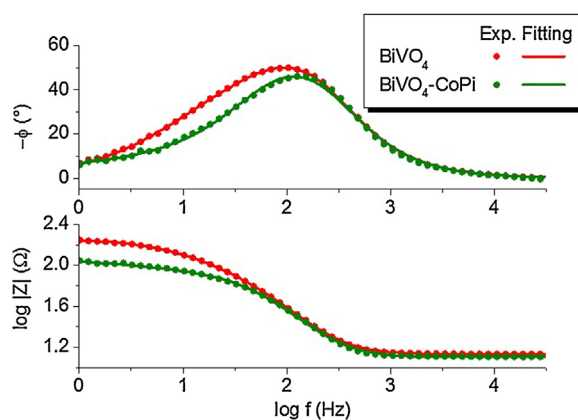


**Fig. 11.** Bode plots of the EIS measurements (symbols) acquired at 1.23 V<sub>RHE</sub> under visible light irradiation (100 mW cm<sup>-2</sup>) and data fitted (lines) with the same equivalent circuit depicted in the inset in Fig. 7.

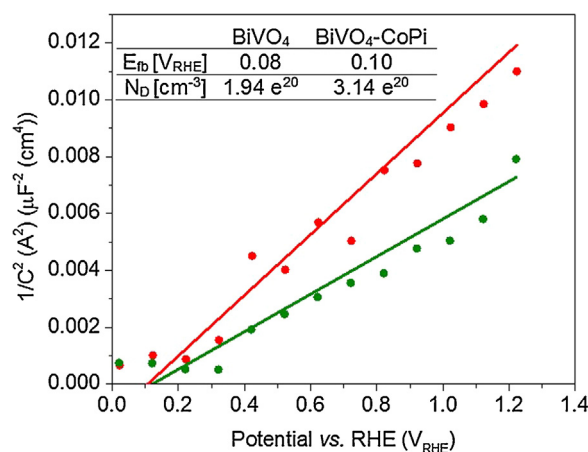


**Fig. 12.** Mott-Schottky plots of dense BiVO<sub>4</sub> and BiVO<sub>4</sub>-CoPi photoanodes. Data recorded at a constant frequency of 5 kHz.

with an increase in the  $k_{tr}/k_{rec}$  ratio, thus indicating a good equivalence between the two approaches used to evaluate the reaction kinetics on the here studied BiVO<sub>4</sub> photoelectrodes. Nevertheless, although EIS remains the most commonly adopted method for the evaluation of the recombination phenomena, transient photocurrent analysis has been found to be an easy and fast method that can provide equivalent results and could allow a preliminary evaluation of photoanode efficiency to be established in a short time.

Finally, in order to elucidate how CoPi affects the photoanode bulk properties, the flat band potentials ( $E_{fb}$ ) and donor density ( $N_D$ ) values of both photoanodes were extrapolated from the Mott-Schottky plots (see Fig. 12). It can be noted that CoPi, deposited on the BiVO<sub>4</sub> surface, does not influence the flat band potential to any great extent, but gives rise to a higher donor density in the photoanode where it is present. Such a result can be explained by considering that a higher mobility of  $e^-$  is induced indirectly by the previously explained lower superficial recombination of charges, which is a consequence of the enhanced water oxidation ( $h^+$ ) reaction kinetics on the CoPi-catalyzed BiVO<sub>4</sub> photoelectrode. However, even though the rate of the water oxidation half-reaction is increased to a great extent, the poor electron transport within the BiVO<sub>4</sub> bulk film still limits the overall efficiency of the here reported BiVO<sub>4</sub>-CoPi photoanodes, compared to other works on cation or anion doped-BiVO<sub>4</sub> [22,53], due to the accumulation of electrons in the CB and their consequent recombination. Therefore, it remains crucial to combine modification techniques or to explore new ways of directly injecting the



photo-generated electrons within the BiVO<sub>4</sub> into other materials [18,23,24], in which they could move extremely fast and suppress the recombination.

#### 4. Conclusions

In this work, BiVO<sub>4</sub> thin films with a scheelite-monoclinic phase and of similar thicknesses but different morphologies (dense and porous) have been synthesized, by means of the spin-coating technique, on FTO-coated glasses (confirmed by XRD, FESEM and UV–vis spectroscopy analyses). It has resulted, from the photoelectrochemical tests, that the dense BiVO<sub>4</sub> morphology has a lower superficial recombination rate than the porous one, and up to 3.5 times higher photocurrent densities can be achieved with such a material. The analyses of the transient photocurrents and of the EIS measurements (exploiting an equivalent circuit) have furnished equivalent conclusions: regardless of the exposed surface area of the BiVO<sub>4</sub> photoanodes, the charge transfer kinetics in the dense material is about 3-fold faster than the one on the porous film. In the present case, a slower electrons transport and a probably higher concentration of defective states in the grain boundaries of the porous film could be the cause of the increased surface recombination phenomenon. Although more detailed studies on this aspect still need to be carried out, it is important to point out that the optimization of the BiVO<sub>4</sub> synthesis method, in order to avoid multiple processing steps that can cause defects in the structure of the film, is fundamental to increase the performance of the BiVO<sub>4</sub> material.

On the other hand, the achievement of the PED of CoPi in an optimized time of 60 s (under sunlight illumination) has led to a 5-fold increase in the photocurrent generation of the dense BiVO<sub>4</sub> film, thus yielding an enhancement of 70% in the charge transfer kinetics, which has confirmed the role of CoPi as an effective water oxidation catalyst. Nevertheless, a higher efficiency of the BiVO<sub>4</sub>-CoPipphotoanode was observed when it was only illuminated in the central area (<1 cm<sup>2</sup>), as the double of the photocurrent was achieved at 1.23 V<sub>RHE</sub> (~3 mA/cm<sup>2</sup>) with respect to the total illuminated area of 6 cm<sup>2</sup>. Even though this effect could be related to a higher concentration of defects at the borders of the spin-coated electrode or to a non-uniform morphology of the BiVO<sub>4</sub> over the surface of the film, it raises the issues towards the preparation of large-sized BiVO<sub>4</sub>-based electrodes for practical applications of this material on PECs. Hence, exploring new and more efficient synthesis methods (e.g. sputtering, electrodeposition, etc) that are able to produce uniform BiVO<sub>4</sub> films (on chemical, structural and electronic properties) over extensive deposition areas, and investigating the easiest way to tune their bulk and superficial properties (i.e. by doping, creating heterojunctions or co-catalyzing), for the fabrication of high-performance photoanodes, remain challenges that still have to be faced.

#### Acknowledgements

The authors would like to thank the European Commission, 7th Framework Program (NMP-2012 Project Eco<sup>2</sup>CO<sub>2</sub> nr.309701 and FCH-JU Call 2011-1 Project ArtipHyction nr.303435), for the financial support. Thanks are due to Marco Fontana and Mauro Raimondo for the FESEM analyses reported in the ESI section.

#### Appendix A. Supplementary data

Supplementary data (i.e. ESI) associated with this article can be found, in the online version, at <http://dx.doi.org/10.1016/j.apcatb.2016.02.059>.

#### References

[1] A. Thapper, S. Styring, G. Saracco, A.W. Rutherford, B. Robert, A. Magnuson, W. Lubitz, A. Llobet, P. Kurz, A. Holzwarth, *Green* 3 (2013) 43–57.

[2] M.S. Préfot, K. Sivula, *J. Phys. Chem. C* 117 (2013) 17879–17893.  
 [3] M.W. Kanan, D.G. Nocera, *Science* 321 (2008) 1072–1075.  
 [4] A. Kudo, Y. Miseki, *Chem. Soc. Rev.* 38 (2009) 253–278.  
 [5] S. Hernández, S.M. Thalluri, A. Sacco, S. Bensaid, G. Saracco, N. Russo, *Appl. Catal. A: Gen.* 504 (2015) 266–271.  
 [6] A. Kudo, K. Ueda, H. Kato, I. Mikami, *Catal. Lett.* 53 (1998) 229–230.  
 [7] C. Martínez Suarez, S. Hernández, N. Russo, *Appl. Catal. A: Gen.* 504 (2015) 158–170.  
 [8] Z. Zhao, Z. Li, Z. Zou, *Phys. Chem. Chem. Phys.* 13 (2011) 4746–4753.  
 [9] K. Maeda, *J. Photochem. Photobiol. C: Photochem. Rev.* 12 (2011) 237–268.  
 [10] Y. Park, K.J. McDonald, K.-S. Choi, *Chem. Soc. Rev.* 42 (2013) 2321–2337.  
 [11] S. Tokunaga, H. Kato, A. Kudo, *Chem. Mater.* 13 (2001) 4624–4628.  
 [12] S.M. Thalluri, C.M. Suarez, M. Hussain, S. Hernandez, A. Virga, G. Saracco, N. Russo, *Ind. Eng. Chem. Res.* 52 (2013) 17414–17418.  
 [13] Y. Liang, T. Tsubota, L.P. Mooij, R. van de Krol, *J. Phys. Chem. C* 115 (2011) 17594–17598.  
 [14] F.F. Abdi, R. van de Krol, *J. Phys. Chem. C* 116 (2012) 9398–9404.  
 [15] S.M. Thalluri, S. Hernández, S. Bensaid, G. Saracco, N. Russo, *Appl. Catal. B: Environ.* 180 (2016) 630–636.  
 [16] R.M.N. Yerga, M.C.A. Galvan, F. del Valle, J.A.V. de la Mano, J.L.G. Fierro, *ChemSusChem* 2 (2009) 471–485.  
 [17] W. Yao, H. Iwai, J. Ye, *Dalton Trans.* 11 (2008) 1426–1430.  
 [18] P.M. Rao, L. Cai, C. Liu, I.S. Cho, C.H. Lee, J.M. Weisse, P. Yang, X. Zheng, *Nano Lett.* 14 (2014) 1099–1105.  
 [19] X.K. Wang, G.C. Li, J. Ding, H.R. Peng, K.Z. Chen, *Mater. Res. Bull.* 47 (2012) 3814–3818.  
 [20] S.M. Thalluri, C. Martínez Suarez, S. Hernández, S. Bensaid, G. Saracco, N. Russo, *Chem. Eng. J.* 245 (2014) 124–132.  
 [21] S.K. Pilli, T.E. Furtak, L.D. Brown, T.G. Deutsch, J.A. Turner, A.M. Herring, *Energy Environ. Sci.* 4 (2011) 5028–5034.  
 [22] F.F. Abdi, L. Han, A.H. Smets, M. Zeman, B. Dam, R. van de Krol, *Nat. Commun.* 4 (2013).  
 [23] Y.H. Ng, A. Iwase, A. Kudo, R. Amal, *J. Phys. Chem. Lett.* 1 (2010) 2607–2612.  
 [24] Y. Cheng, C. Xu, L. Jia, J.D. Gale, L. Zhang, C. Liu, P.K. Shen, S.P. Jiang, *Appl. Catal. B: Environ.* 163 (2015) 96–104.  
 [25] D. Hidalgo, R. Messina, A. Sacco, D. Manfredi, S. Vankova, E. Garrone, G. Saracco, S. Hernández, *Int. J. Hydrogen Energy* 39 (2014) 21512–21522.  
 [26] G. Li, D. Zhang, J.C. Yu, *Chem. Mater.* 20 (2008) 3983–3992.  
 [27] W. Yin, W. Wang, M. Shang, L. Zhou, S. Sun, L. Wang, *Eur. J. Inorg. Chem.* 2009 (2009) 4379–4384.  
 [28] S.M. Thalluri, R.M. Rojas, O.D. Rivera, S. Hernandez, N. Russo, S.E. Rodil, *Phys. Chem. Chem. Phys.* 17 (2015) 17821–17827.  
 [29] J.A. Seabold, K.S. Choi, *J. Am. Chem. Soc.* 134 (2012) 2186–2192.  
 [30] M.W. Kanan, Y. Surendranath, D.G. Nocera, *Chem. Soc. Rev.* 38 (2009) 109–114.  
 [31] M.W. Kanan, J. Yano, Y. Surendranath, M. Dinca, V.K. Yachandra, D.G. Nocera, *J. Am. Chem. Soc.* 132 (2010) 13692–13701.  
 [32] T.H. Jeon, W. Choi, H. Park, *Phys. Chem. Chem. Phys.* 13 (2011) 21392–21401.  
 [33] L. Peter, *J. Solid State Electrochem.* 17 (2013) 315–326.  
 [34] K. Gelderman, L. Lee, S. Donne, *J. Chem. Educ.* 84 (2007) 685.  
 [35] S. Hernández, V. Cauda, A. Chiodoni, S. Dallorto, A. Sacco, D. Hidalgo, E. Celasco, C.F. Pirri, *ACS Appl. Mater. Interfaces* 6 (2014) 12153–12167.  
 [36] E.M. Steinmiller, K.-S. Choi, *Proc. Natl. Acad. Sci. U. S. A.* 106 (2009) 20633–20636.  
 [37] D. Wang, R. Li, J. Zhu, J. Shi, J. Han, X. Zong, C. Li, *J. Phys. Chem. C* 116 (2012) 5082–5089.  
 [38] D. Grosso, *J. Mater. Chem.* 21 (2011) 17033–17038.  
 [39] H. Fan, T. Jiang, H. Li, D. Wang, L. Wang, J. Zhai, D. He, P. Wang, T. Xie, *J. Phys. Chem. C* 116 (2012) 2425–2430.  
 [40] S. Obregon, G. Colon, *Catal. Sci. Technol.* 4 (2014) 2042–2050.  
 [41] I.D. Brown, K.K. Wu, *Acta Crystallogr. B* 32 (1976) 1957–1959.  
 [42] S.M. Thalluri, C. Martínez Suarez, M. Hussain, S. Hernandez, A. Virga, G. Saracco, N. Russo, *Ind. Eng. Chem. Res.* 52 (2013) 17414–17418.  
 [43] L.M. Peter, D. Vanmaekelbergh, *Advances in Electrochemical Science and Engineering*, Vol. 6, Wiley-VCH Verlag GmbH, 2008, pp. 77–163.  
 [44] L.M. Peter, J. Li, R. Peat, *J. Electroanal. Chem. Interfacial Electrochem.* 165 (1984) 29–40.  
 [45] B. Klahr, S. Gimenez, F. Fabregat-Santiago, T. Hamann, J. Bisquert, *J. Am. Chem. Soc.* 134 (2012) 4294–4302.  
 [46] L. Badia-Bou, E. Mas-Marza, P. Rodenas, E.M. Barea, F. Fabregat-Santiago, S. Gimenez, E. Peris, J. Bisquert, *J. Phys. Chem. C* 117 (2013) 3826–3833.  
 [47] J. Bisquert, G. Garcia-Belmonte, F. Fabregat-Santiago, N.S. Ferriols, P. Bogdanoff, E.C. Pereira, *J. Phys. Chem. B* 104 (2000) 2287–2298.  
 [48] S. Hernández, M. Tortello, A. Sacco, M. Quaglio, T. Meyer, S. Bianco, G. Saracco, C.F. Pirri, E. Tresso, *Electrochim. Acta* 131 (2014) 184–194.  
 [49] A. Walsh, Y. Yan, M.N. Huda, M.M. Al-Jassim, S.-H. Wei, *Chem. Mater.* 21 (2009) 547–551.  
 [50] J. Yu, A. Kudo, *Adv. Funct. Mater.* 16 (2006) 2163–2169.  
 [51] D. Wang, H. Jiang, X. Zong, Q. Xu, Y. Ma, G. Li, C. Li, *Chem. A Eur. J.* 17 (2011) 1275–1282.  
 [52] R. Li, F. Zhang, D. Wang, J. Yang, M. Li, J. Zhu, X. Zhou, H. Han, C. Li, *Nat. Commun.* 4 (2013) 1432.  
 [53] T.W. Kim, Y. Ping, G.A. Galli, K.-S. Choi, *Nat. Commun.* 6 (2015) 1–10.